Modelling the Impact of Alloying State Dynamics on-the Reactivity of Group-10-Metal-Gallium Nanoparticles.

Quentin Pessemesse, Alexandre Perochon, Christophe Copéret, Marie-Eve Perrin, Pierre-Adrien Payard

Modelling the Impact of Alloying State Dynamics on-the Reactivity of Group-10-Metal-Gallium Nanoparticles

Quentin Pessemesse,[1,2] Alexandre Perochon,[1] Christophe Copéret,*[2] Marie-Eve L. Perrin,*[1] Pierre-Adrien Payard*[1,3]

[1] Universite Claude Bernard Lyon I, CNRS, CPE-Lyon, UMR 5246, ICBMS, 1 rue Victor Grignard, F-69622 Villeurbanne Cedex, France

[2] ETH Zurich, Department of Chemistry and Applied Biosciences, Vladimir-Prelog Weg 1-5/10, CH-8093 Zurich, Switzerland

[3] Dunia Innovations, Magnusstraße 11, 12489 Berlin, Germany

Ab intio Molecular Dynamics, Blue Moon Sampling, Group 10 Metals, Gallium, Nanoparticles, Catalysis

ABSTRACT: Bimetallic nanoparticles are catalysts for reactions, such as CO_x hydrogenation or propane dehydrogenation. Recently, gallium has been identified as a promoter which enables dispersion of group-X-metal sites, raising activity and selectivity. However, quantitative information on alloying dynamics under reaction conditions are not readily available and a general computational method to access such information is missing. Here, an *ab initio* molecular dynamics workflow with enhanced sampling methods is used to probe the alloying behavior of Ni-, Pd-, and Pt-Ga nanoparticles under operating conditions (T = 600°C) in presence of H_2 or CO. The three metals display different alloying behaviors with Ga: Ni forms a core surrounded by gallium, while Pd and Pt form different alloyed structures. Both H_2 and CO shift the alloying state to different extents. A set of three descriptors is proposed to compare and quantify the alloying behavior of these catalyst models: (i) the position α^{min} of the most stable alloying state; (ii) the curvature η_α of the free energy at α^{min}, referred to as the alloying hardness; (iii) the skew κ_α of the free energy at α^{min}, which relates to its propensity to alloy or segregate. The influence of the alloying behavior on the propane dehydrogenation activity of NiGa and PtGa is assessed: the energetic cost of alloy reorganization in the activation energy has been quantified. Extracting quantitative alloying descriptors from *ab initio* molecular dynamics is a promising tool to take alloy reorganization into account, both for mechanistic studies and for rational catalyst design.

INTRODUCTION

Supported bimetallic nanoparticles are ubiquitous catalysts in industrial chemical processes as they typically show improved performances (activity, selectivity and/or stability) compared to monometallic systems. One prominent example is the Oleflex propane dehydrogenation (PDH) process, which relies on PtSn-based supported catalysts.[1,2,3] Compared to pure Pt, the presence of Sn as a promoter slows deactivation through coking and sintering,[4,5] and improves selectivity toward the desired propene product. Similarly, Pt-based PDH catalysts are improved by the addition of Ga as a promoter,[6] and were recently implemented in industrial settings.[7,8,9,10,11,12] PdGa and NiGa have also been studied in the context of PDH. PdGa displays significantly lower activity and faster deactivation than PtGa ($k_d \sim 10^2$ *vs* 10^{-2} h^{-1}),[13] while NiGa also favors propane cracking yielding ethylene and methane in place of the desired propene and H_2 products.[14,15] Notably, the introduction of Ga to group 10 metals can also switch their established selectivity in other reactions such as in CO_2 hydrogenation. In the absence of promoter group 10 metals are established catalysts for the reverse water–gas shift reaction (Pt,[16,17] Pd[18]) and for CO_2 methanation (Ni[19]). They however become selective toward methanol formation in the presence of Ga.[20,21,22]

These different reactivity patterns cannot be readily understood without an understanding of the dynamic structure of these catalysts. The changes in activity, stability and selectivity of these active metals (Ni, Pd, Pt) upon the addition of promoters such as Ga correlate with the formation of alloyed bimetallic nanoparticles evidenced by X-Ray adsorption spectroscopy.[23,24,22,21]

The alloying state in bimetallic catalysts can be probed using H_2 or CO chemisorption, where a reduced surface coverage is measured in the presence of a Ga additive. This is typically interpreted as a decrease in available transition metal sites on the surface due to alloying dilution.[5,22] In addition, infrared spectroscopy under CO atmosphere indicates a lower number of bridging CO molecules in the presence of Ga, consistent with the formation an alloy. These characterization data show that the transition metal atoms are dispersed in a Ga matrix, resulting in the formation of isolated sites.

However, both the precise nature of the alloy and the chemical environment of the metal sites under reactive atmospheres remain unknown. Indeed, the alloying state determined by chemisorption experiments does not necessarily reflect the alloying state under reaction conditions (high temperature, pressure, and presence of reactants, products and intermediates). Probe molecules, reactants and reaction intermediates can induce a restructuration of the catalyst.[25,26,27] *In situ* and *operando* spectroscopic measurements have

been performed to characterize the chemical environment of the active site under reaction conditions. The incorporation of Ga(0) in group-10-metal nanoparticles under both PDH and CO_2 hydrogenation to methanol conditions has been confirmed by X-ray absorption spectroscopy. **Erreur ! Signet non défini.,Erreur ! Signet non défini.,Erreur ! Signet non défini.,**[28] However, identifying the geometry and composition of the environment around the metal sites from spectroscopy is not straightforward. To address this issue, *operando* modelling,[29] that is modelling the structure of the catalyst under operating conditions, serves as a valuable tool both in exploratory studies, and as a support to interpret experimental findings.

Computational approaches to understand heterogeneous bimetallic catalysts usually rely on infinite slab models using periodic DFT calculations.[30,31] These models bias the distribution of surface sites, in particular underestimating defect proportion as well as excluding dynamic restructuring of the system, i.e. the nano-scale restructuration of the catalyst due to the interaction with the support and adsorbates under operating conditions.[32] These phenomena are particularly prominent in highly dynamic bimetallic nanoparticles (< 2 nm). A given alloying state consists of an ensemble of structures with a common extent of alloying (*vide infra*). Thus, molecular dynamics simulations on small nanoparticle models are well-suited to sample these ensembles, and intrinsically recover most entropy contributions, including configurational entropy.[33] In addition, nanoparticle models include edge & vertex sites as well as other defects that are often absent in slab models. In this context, molecular dynamics simulations using parametrized force fields were fruitfully used to investigate segregation in nano-alloys,[34,35] but this approach remains ill-suited to the investigation of adsorbates and their surface reactivity.

In that context, the *ab initio* molecular dynamics (AIMD) approach is well-suited to investigate the link between the alloying behavior of bimetallic catalysts and their activity. Due to the high computational cost of the method, the sampling must be enhanced to explore relevant structures on a reasonable time scale. Enhances sampling methods were implemented to model Mn segregation within PtMn-based nanoparticles, which proved useful to understand the X-ray absorption signature of the catalyst.[36] Similarly, the alloying state of PdGa-based CO_2 dehydrogenation catalysts could be gathered from AIMD studies.[37] Regarding the PtGa-based catalysts, its high propylene selectivity in PDH was linked to the isolation of Pt sites that favor propylene desorption over deep dehydrogenation to coke.[38] The coking pathway was correlated with partial dealloying of the catalyst, but the phenomenon was not quantified as the alloying state was not explicitly sampled. Although fruitful information could be gathered from these simulations, only qualitative conclusions were drawn due to the convergence rate limitation of metadynamics as a sampling method and the inefficient sampling of the alloying state.

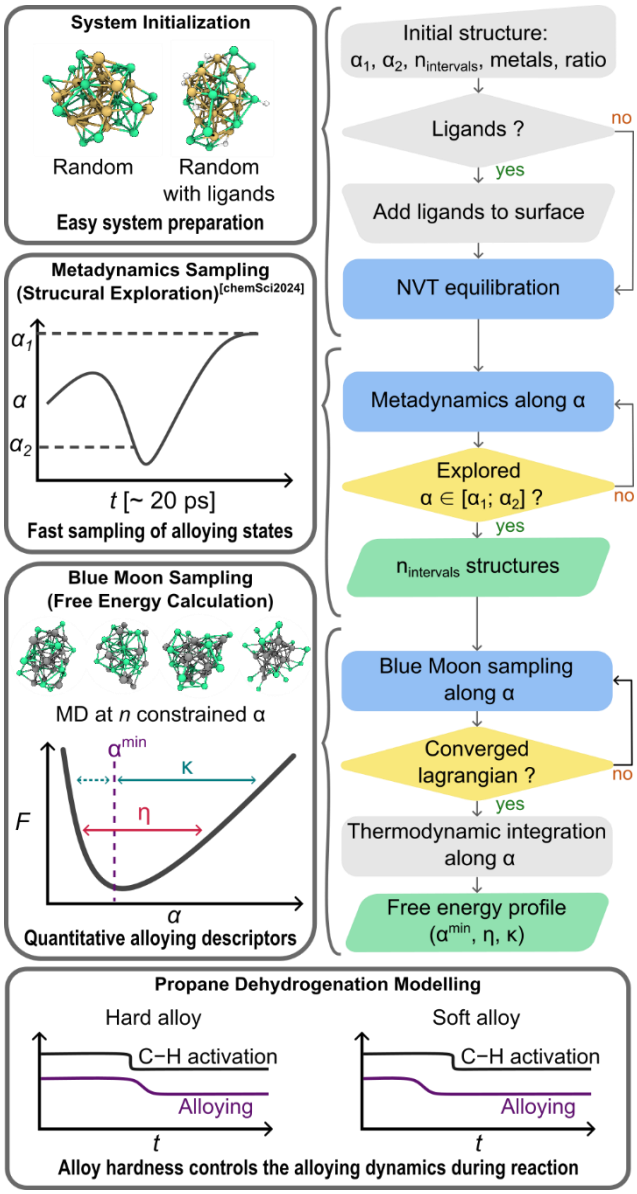

Figure 1. Computational workflow to model the alloying dynamics of nanoparticles.

A computational methodology that goes beyond these limitations is required to probe the influence of alloying on the structure and reactivity of bimetallic catalysts (**Figure 1**). This methodology consists in a preliminary biased AIMD simulation (metadynamics[39]) using a single alloying parameter. This ensures the exploration of representative structures for alloying states ranging from alternating to segregated alloys. Selected structures are then used as starting points for free energy calculations (Blue Moon sampling[40]). This method provides quantitative insight into alloying-dealloying processes in nanometer-sized particles (36 atoms, *i.e.* ~ 1 nm), under relevant operating conditions of temperature (T = 600 °C) and adsorbate composition (vacuum, CO, H_2). In the case of Ni-, Pd-, and Pt-Ga systems, a set of quantitative statistical descriptors related to alloying was extracted from AIMD simulations, unlocking simulations that quantify the influence of the alloying – dealloying process on the energy barriers.

COMPUTATIONAL DETAILS

$M_{18}Ga_{18}$ structures of approximately 1 nm in diameter were generated using Packmol.[41] While real catalysts have dispersity both in size and composition, this model was deemed sufficient to explore relevant alloying states and extract descriptors of catalytic activity. The structures were equilibrated using at least 2 ps of unbiased *ab initio* Molecular Dynamics (AIMD) in the NVT ensemble at the DFT level (see ESI for the full computational details).

Metadynamics[39] simulations were ran for 10 to 20 ps, starting from the equilibrated structures. The history-dependent bias was deposited along single collective variable, which was designed by taking inspiration from Cowley's short range order parameter α.[42] We define it as such (**Eq. 1**):

$$\alpha = 1 - 2 \times \sum_{\mathrm{M}} \frac{CN(\mathrm{M}-\mathrm{Ga})}{CN(\mathrm{M}-\mathrm{Ga}) + CN(\mathrm{M}-\mathrm{M})}, (1)$$

where M = Ni, Pd, Pt and *CN*(X–Y) is defined as the following switch function based on interatomic distances (**Eq. 2**):

$$CN(X-Y) = \frac{1}{N_X}\sum_{i\in X}\sum_{i\in Y}\frac{1-\left(\frac{r_{ij}}{R_0}\right)^{NN}}{1-\left(\frac{r_{ij}}{R_0}\right)^{ND}}, (2)$$

where r_{ij} is the distance between atoms i and j, and R_0 is the critical length of the X–Y bond, taken to be 130% of the atomic radii. This collective variable represents the size of the interface between M and Ga. It is equivalent to a previously reported segregation parameter.[43] Three notable cases are: the alternating alloy: α = –1, the segregated structure: α = +1, and the entropic alloy: α = 0. While efficient exploration of the CV space is observed, this method suffers from slow convergence, making appropriate convergence out of reach given the computational cost of AIMD. Larger sets of collective variables led to much slower convergence, while multiple walkers metadynamics simulations led to unphysical behavior before convergence could be achieved (see ESI). To solve the convergence issue of metadynamics, structures were selected from metadynamics runs to carry out Blue Moon sampling of the free energy surface (see ESI). Appropriate convergence of the Blue Moon sampling simulations was assumed after 5 ps of simulation. While this method is as computationally expensive as metadynamics, its fast convergence and ideal parallelization makes it a great match to extract quantitative information on 1 nm scale metallic nanoparticles. Given the importance of supported gallium-doped group-10-metal nanoparticles in catalysis, this workflow was used to probe the atomic structure of $Ni_{18}Ga_{18}$, $Pd_{18}Ga_{18}$ and $Pt_{18}Ga_{18}$ models. Principal component regression of the free energy surface was used to interpret the results of the Blue Moon sampling simulations using the Scikit-Learn Python package.

RESULTS AND DISCUSSION

Alloying and dynamics of Metal-Gallium nanoparticles. $Ni_{18}Ga_{18}$, $Pd_{18}Ga_{18}$ and $Pt_{18}Ga_{18}$ models were studied using the developed workflow which relies on metadynamics exploration followed by thermodynamic integration (*vide supra*). The sampling methods rely on a collective variable (CV) inspired by Cowley's short range order parameter α (**Eq. 1**),[42] which takes negative values for alloyed systems and positive ones for segregated ones. This workflow yields a free energy surface as a function of α for each system.

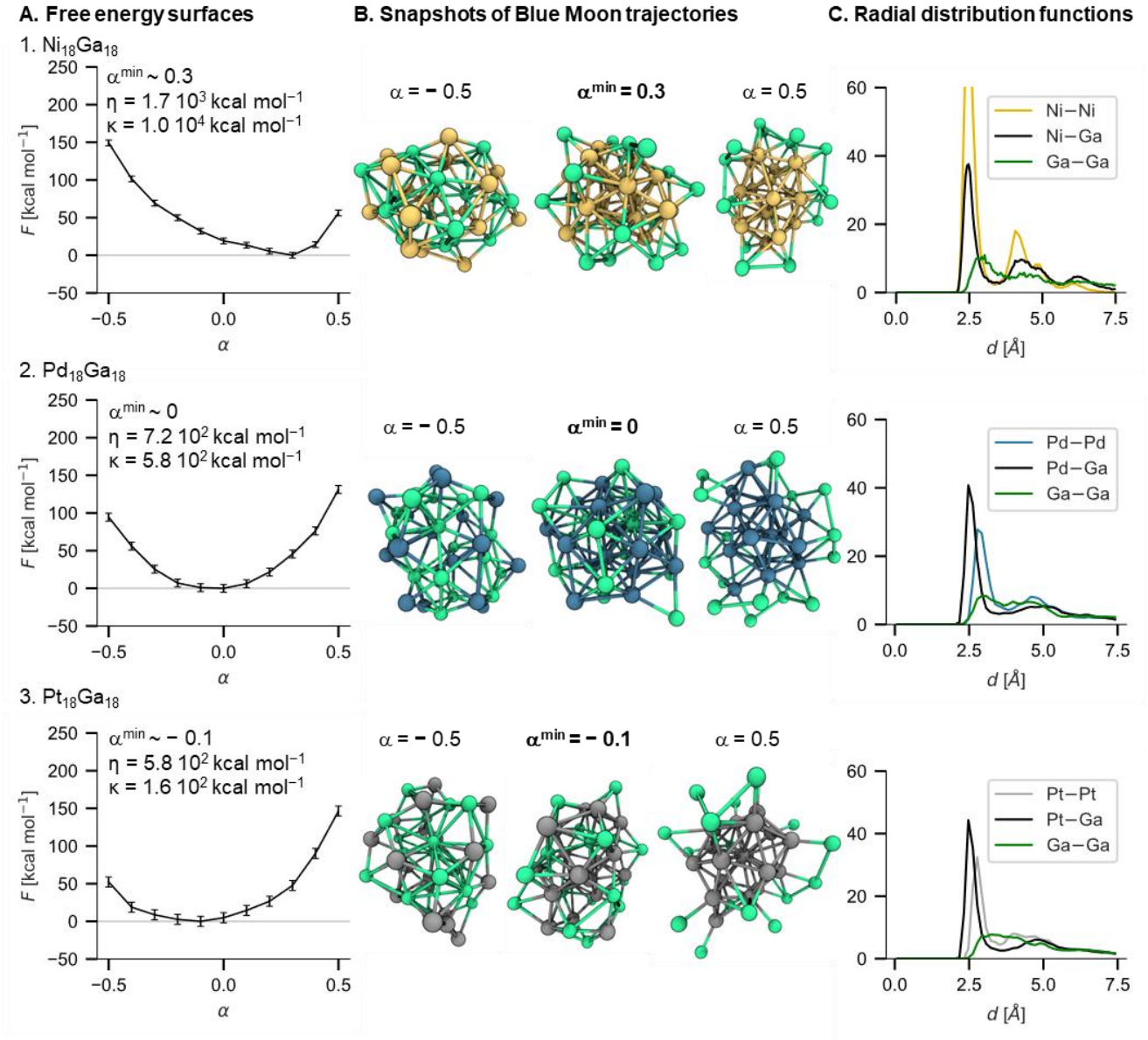

Figure 2. **A.** Free energy surfaces obtained from thermodynamic integration in the Blue Moon ensemble. **B.** Snapshots of Blue Moon sampling trajectories for selected values of α. **C.** Radial distribution functions for the minimum free energy trajectory. Color coding: Ni – yellow; Pd – blue; Pt – grey; Ga – green.

Table 1.1 Values of alloy position(α^{min}), alloying hardness (η) and skew (κ) for each of $M_{18}Ga_{18}L_9$ model, L = none, H, CO; M = Ni, Pd, Pt.

	$Ni_{18}Ga_{18}L_9$			$Pd_{18}Ga_{18}L_9$			$Pt_{18}Ga_{18}L_9$		
L	none	H_9	$(CO)_9$	none	H_9	$(CO)_9$	none	H_9	$(CO)_9$
a^{min}	0.3	0.1	0	0	− 0.1	− 0.2	− 0.1	− 0.1	− 0.1
η [kcal mol^{-1}]	1740	1233	1043	715	1165	1025	580	1043	808
κ [kcal mol^{-1}]	10138	− 12.5	− 1238	575	− 1475	-1000	313	− 2313	313

We consider three descriptors to capture the bimetallic nanoparticle's alloying behavior from the free energy surface along the alloying parameter α. First, the α^{min} value, which corresponds to the minimum of the FES, can be referred to as the alloy position (**Figure 1**). It indicates the most stable alloying state. Next is the curvature (second derivative) η of the FES at α^{min}, which refers to as the alloying hardness. It represents the energetic cost associated to a change in the alloying state. The concept is in analogy with Pearson's and Parr's definition of chemical hardness where the second derivative of the energy with respect to the number of electrons captures the ease of deformation of the electron cloud or polarizability.[44] Last is the third derivative κ of the FES at α^{min}, referred to as the alloy's skew. It indicates the difference in alloying hardness in either direction away from α^{min}; positive values indicate easier alloying, and negative values indicate easier segregation. These three descriptors are characteristic of a given alloying behavior (**Figure 1**). At first glance, the three systems display different alloying behavior (**Figure 2.A** and **2.B**). The $Ni_{18}Ga_{18}$ model, with a single global free energy minimum obtained for $\alpha^{min} \sim 0.3$, is the least alloyed and corresponds to a core-shell-type structure (**Figure 2.B.1**). In contrast, $Pt_{18}Ga_{18}$ converges with $\alpha^{min} \sim -0.1$ and is thus the most alloyed system (**Figure 2.B.2**), while $Pd_{18}Ga_{18}$ with $\alpha^{min} \sim 0$ displays an intermediate behavior between Ni and Pt (**Figure 2.B.3**). The results for the PdGa and PtGa systems are in good agreement with experimental EXAFS data as well as with previous MD and MTD calculations performed on similar systems.[36,38] In addition, the unique core-shell structure of NiGa was not previously discussed, due to the larger nanoparticles size obtained in prepared catalysts.[21]

The three systems display variable free energy costs for alloying-segregation processes, as described by hardness η and skew κ parameters (**Figure 1**, **Table 1**). The hardness across the series increases as follows: $Pt_{18}Ga_{18}$ ($\eta_{PtGa} = 5.8\ 10^2$ kcal mol^{-1}) < $Pd_{18}Ga_{18}$ ($\eta_{PdGa} = 7.2\ 10^2$ kcal mol^{-1}) < $Ni_{18}Ga_{18}$ ($\eta_{NiGa} = 1.7\ 10^3$ kcal mol^{-1}). The skew κ is positive for all systems, indicating that further alloying is more favorable than dealloying, albeit less and less going from Ni to Pt ($\kappa_{NiGa} = 10138$ kcal mol^{-1} > $\kappa_{PdGa} = 575$ kcal mol^{-1} > $\kappa_{PtGa} = 163$ kcal mol^{-1}). Down the group 10 column, $M_{18}Ga_{18}$ nanoparticles become more alloyed, softer, and less skewed toward alloying (lower α^{min}, η and κ as reported in **Table 1**).

Given the high temperature of the simulation (600°C), significant thermal disorder is expected, and melting of bimetallic nanoparticles has been reported at these temperatures.[45] The radial distribution functions for the most stable alloying state was used to investigate the disorder and crystallinity of these small nanoparticle models. $Ni_{18}Ga_{18}$ is the most ordered of the three systems, with well-defined first and second coordination spheres around Ni (sharp peaks at $r_0^{Ni\text{-}Ni} = r_0^{Ni\text{-}Ga} = 2.5$ Å and $r_1^{Ni\text{-}Ni} = r_2^{Ni\text{-}Ga} = 4.7$ Å). This organization is dynamic, as revealed by the lower ordering of Ga in the first and second sphere of Ni (**Figure 2.C.1**). In contrast, $Pd_{18}Ga_{18}$ and $Pt_{18}Ga_{18}$ only display ordered M-M and M-Ga first spheres (**Figure 2.C.2.** and **C.3;** sharp peaks only at $r_0^{M\text{-}Ga} = 2.5$ Å and $r_0^{M\text{-}Ga} = 2.6$). Their M-M and M-Ga second spheres are very disordered, and Ga-Ga coordination is "liquid-like" (no sharp peaks even in the first sphere).

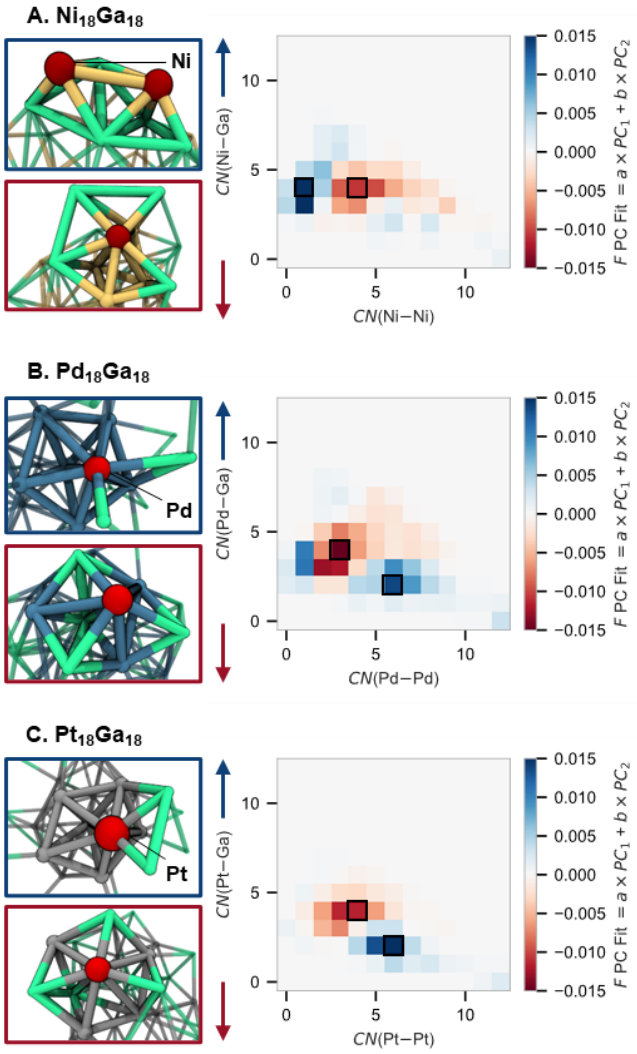

Figure 3. Coefficients of the principal component regression of the free energy surface, correlating to the free energy of individual coordination environments for the metal sites. Snapshots corresponding to typically favored (red box) and disfavored (blue box) metal sites (in red).

Alloying Analyses. The important changes in alloying behaviors of bimetallic nanoparticles relate to the varying stability of different metal atoms in given coordination environments. A principal component regression (PCR) methodology was used to identify the discrete sites that are responsible for a given alloying state. The free energy as a function of the alloying state $F(\alpha)$ was fitted with the first two principal components of the distribution of M–M and M–Ga coordination numbers along each constrained MD trajectory (See ESI for a detailed discussion of the PCR methodology). The weighted coefficient of each type of site in the principal component fit for each type of noble metal site represents their correlation with the alloying free energy.

The alloying behaviors of Ni-, Pd- and Pt- based alloys can be traced back to ensembles of stable (negative coefficients) and unstable sites (positive coefficients). In the case of $Ni_{18}Ga_{18}$, high-Ni-coordinated sites are relatively stable (**Figure 3.A**; sites with negative coefficients are at or below the *CN*(M-Ga) = *CN*(M-M) diagonal). This favors the formation of a core-shell type structure. The distribution of coefficients for $Pd_{18}Ga_{18}$ is more symmetrical: both high Ga- and high-Pd coordination is disfavored, leading to an entropic alloy (**Figure 3.B**; sites with positive coefficients are away from the diagonal). $Pt_{18}Ga_{18}$ organizes in an alternating alloy due to the increased stability of sites with a high Ga coordination (**Figure 3.C**; sites with positive coefficients are at or above the diagonal). These quantitative descriptors point to which type of site is correlated to a stable alloying state.

The coefficients of the two components of the FES fit provide additional information on the origin of this stability difference. The first component (a × PC1, **ESI figures**) is linear with α, and takes opposite signs for high-M coordination spheres compared to high-Ga ones. This component seemingly captures the difference in bonding energy between homometallic and heterometallic bonds. For the Ni-based alloy, the formation of homometallic bonds is energetically favored, while heterometallic bonds are energetically favored in Pt-based alloys. In the case of the Pd-based alloy, the first principal component has a negligible weight in the FES fit: Pd-Ga and Pd-Pd bonds seem nearly isoenergetic in this case, and the alloy is entropically driven.

The second component of the fit (b × PC2, **ESI figures**) takes more negative values for the entropically favored CN(M-M) ~ CN(M-Ga) ~ 5 environment. while high Ga or M coordinations around M sites are disfavored. Thereof, PC2 captures the mixing entropy, as

well as the disfavored Ga-Ga interaction, leading to a quadratic distribution skewed toward higher Ga environments for the three studied systems (**ESI figures**). The two components of the fit capture energetic and entropic contributions to the free energy, which helps rationalize the behavior of the different metals in combination with gallium.

Effect of the gas phase composition on alloying state. The developed AIMD workflow herein developed is capable of predicting the alloying behavior of ligandless nanoparticles. However, under chemisorption or catalytic conditions, the adsorption of molecules on the catalyst can induce a reorganization of the catalyst's surface, thereby altering available surface/active sites. Therefore, we have expanded our study to include $M_{18}Ga_{18}L_9$ (M = Ni, Pt, Ga; L = CO, ½ H_2) as a proof of concept to demonstrate the capability of the designed workflow to describe catalyst restructuring under reactive atmospheres (ESI for full computational details). CO and H_2 provide simple models for weak and strong field ligands and are relevant adsorbates in catalysis, as reactants or intermediates. Given the high exergonicity of H_2 dissociation at group-10 metals, adsorbed H_2 is modelled under its hydride form. The coverage was chosen to account to around half of the metal atoms being covered, which is consistent with experimental data for CO-covered PdGa.[46] Metadynamics simulation of the model clusters were carried out using the same parameters as in the ligandless case as depicted above, followed by thermodynamic integration in the blue moon ensemble.

All the studied alloys undergo significant reorganization of the alloying state in the presence of ligands. $Ni_{18}Ga_{18}$ undergoes the most important shift in alloy position under the effect of ligands, with H and CO increasing alloying ($\alpha^{min}(H) \sim 0.1$; $\alpha^{min}(CO) \sim 0$, **Figure 4.A.1**), accompanied by decreased alloying hardness. This translates into a stark modification of the radial distribution function: the second sphere of Ni becomes more disordered with increasing ligand field strength (**Figure 4.B.1**). This is consistent with migration of Ni from the bulk, to form islands of ligated Ni surrounded by mobile Ga atoms at the surface of the particle (**Figure 4.C.1**).

Similarly, ligand coordination to $Pd_{18}Ga_{18}$ leads to a more ordered alloyed nanoparticle, with $\alpha^{min}(H) = \alpha^{min}(CO) = 0.1$. A stronger field ligand skews the free energy surface toward lower a values: further alloying of Ga becomes more favorable (**Figure 4.A.2**). The alloying hardness increases with ligand coordination, while the radial distribution function indicates a more disordered second sphere. The reorganization of the first sphere of ligated atoms is responsible for the effect (**Figure 4.B.1**).

$Pt_{18}Ga_{18}$ seems less affected by the presence of ligands than its lighter analogues ($\alpha^{min}(H) = \alpha^{min}(CO) = \alpha^{min}$, **Figure 4.A.3**). Nevertheless, the different skew of the FES indicates that ligation leads to altered alloy dynamics. First, both ligated nanoparticles display higher alloying hardness. Second, core-shell type structures become more disfavored in the ligated particle. In the case of CO, this is accompanied by a further stabilization of the more alloyed structures ($a < 0.1$). This reveals that both H and CO tend to promote more alloying between M and Ga, albeit to different extent, not every alloying state is affected similarly by the different ligands

The coordination of ligands alters the alloying behavior of all three systems, due to the stabilization of certain surface sites. These sites could be identified using PCR of $F(\alpha)$ with the principal components of the distribution of coordination numbers around M (CN(M–M); CN(M–Ga); CN(M–L)). The weighted coefficients of the fit of $F(\alpha)$ indicate which ligandless and liganded sites are stabilizing (**Figure 5**). The difference between the coefficients for CN(M–L) > 0 and for CN(M–L) = 0 is negative for sites which are stabilized by ligands, and *vice versa* (**Figure 5**).

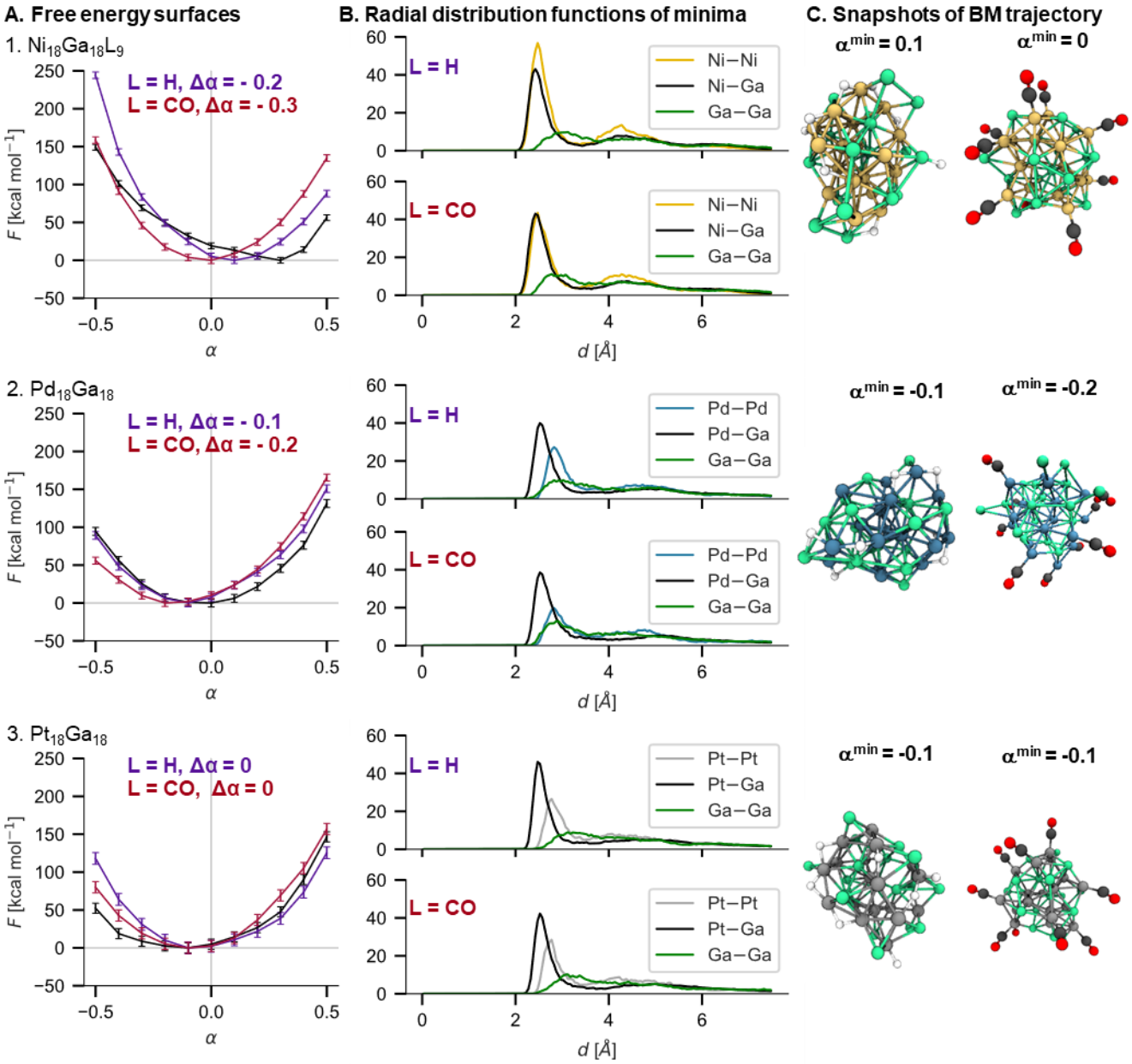

Figure 4. **A**. Free energy surfaces. **B**. Radial distributions. **C**. selected snapshots from the blue moon sampling trajectories for the $M_{18}Ga_{18}L_9$ (M = Ni, Pd, Pt; L = H, CO). Ni – yellow; Pd – blue; Pt – grey; Ga – green, C – dark grey, O – red, H – white.

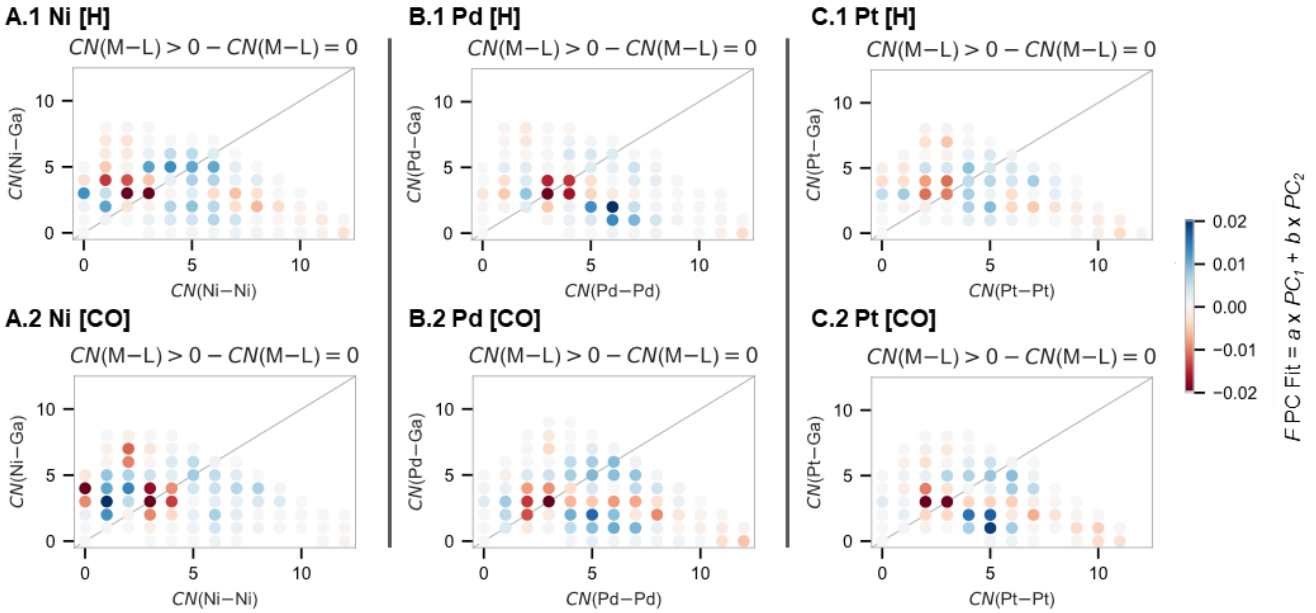

Figure 5. Difference in the coefficients for CN(M–L) > 0 and CN(M–L) = 0 of the principal component fits for $Ni_{18}Ga_{18}L_9$ (**A.**), $Pd_{18}Ga_{18}L_9$ (**B.**) and $Pt_{18}Ga_{18}L_9$ (**C.**), with L = H (**1**) and L = CO (**2**).

The decreased α^{min} of $Ni_{18}Ga_{18}$ after coordination of H can be attributed to the stabilization of 6- and 7-coordinate surface sites with CN(Ni-Ni) ~ CN(Ni-Ga). The even stronger effect of CO can be explained by the stabilization of Ni sites with high-gallium coordination environment, particularly to the 8 to 10 coordinate sites with bulk sites with CN(Ni-Ni) ~ CN(Ni-Ga), and to 4-coordinate surface sites with CN(Ni-Ni) = 0 (**Figure 5.A.2**). We expect the latter sites to be particularly relevant to catalysis as they are very low-coordinate and exposed, making them prime candidates as intermediates in CO activation pathways.

While the FES of $Pd_{18}Ga_{18}$ and $Pt_{18}Ga_{18}$ are less strongly affected by ligand coordination than that of $Ni_{18}Ga_{18}$, PCR suggests that ligands influence the distribution and dynamics of bulk and surface sites. The increased alloying hardness η of $Pd_{18}Ga_{18}$ and $Pt_{18}Ga_{18}$ after ligand coordination is related to the stabilization of sites with close to equal M and Ga coordination. These quantitative PCR descriptors enable the identification of key sites at the surface of the particle.

Alloying dynamics during propane dehydrogenation

As discussed above, the alloying behavior of Ga with group-10-metals differs significantly and is further influenced by the ligands adsorbed on the catalyst surface. This dynamic interaction affects the structure and could influence reaction mechanisms. The segregation of bimetallic alloys has been reported to either increase or decrease the catalytic activity of different bimetallic catalysts.[47,48] Propane dehydrogenation was chosen as a model reaction to study the role of alloying-segregation processes in reaction mechanisms, as previous computational studies suggest that structural changes take place during reactions at the Pt_2Ga surface during the dehydrogenation of propylene to coke precursors.[49] The reaction is also of industrial significance since it enables the conversion of propane-rich shale gas into propene, toward the synthesis of polypropylene.

Metadynamics simulations of propane dehydrogenation on $Ni_{18}Ga_{18}$ and $Pt_{18}Ga_{18}$ were conducted to delineate the influence of alloying-segregation processes on elementary steps on prototypes of soft and hard alloys (see the computational details). The bias was applied on four collective variables: the C–H, C–M and C–C coordination numbers (*CN*), and the α alloying parameter. This set of collective variables enables the exploration of both adsorption and desorption processes (*CN*(C–M)), dehydrogenation (*CN*(C–H)), cracking to carbene, carbyne and carbide intermediates (*CN*(C–C)), and alloying-dealloying processes (α). The metadynamics runs were stopped at the first desorption of propylene.

In the case of $Ni_{18}Ga_{18}$, the simulation reveals a fast dehydrogenation of propane to propene. The reaction starts with the activation of the CH_2 moiety at an isolated Ni surface site. The resulting hydride is rapidly transferred to a neighboring Ni site, yielding an isopropylnickel and a bridging hydride that rapidly diffuses over the particle. C–H activation and alloy reorganization are sequential, and not concerted, as they take place on different time scales (~ 10 fs *vs.* ~ 1 ps). Thereof, the overall reaction barrier for the C–H activation $\Delta F^{\ddagger}$ can be decomposed into contributions from the fast C–H bond cleavage $\Delta_{CH}F^{\ddagger}$ and from the slow alloy reorganization $\Delta_{\alpha}F^{\ddagger}$ (**Figure 6**). The alloying state remains almost constant until the completion of the first C–H bond cleavage, meaning that no reorganization is required to activate the bond. The energetic contribution of the bond cleavage thus dominates the overall energy barrier ($\Delta_{CH}F^{\ddagger}$ = 25.2 kcal mol^{-1} *vs.* $\Delta_{\alpha}F^{\ddagger}$ = 4.0 kcal mol^{-1}, **Figure 7.A**). This reaction is followed by the relaxation of the alloy, consistently with the general trend described in the previous section: hydride ligands promote alloying in $Ni_{18}Ga_{18}$. The second C–H activation is the β-hydride elimination of six methyl H atoms. In contrast with the first step, the cleavage is preceded by a further alloying of the particle, where core Ni atoms migrate into the Ga shell. The presence of Ga is known to increase the electron density at surface group-10-metal sites.[50] A reduced electron density is however known to favor agostic interactions and the subsequent β-hydride elimination in transition metal complexes.[51] Given the high alloy hardness, the reorganization contribution necessary to provide low electron density for the β-hydride elimination dominates the barrier ($\Delta_{\alpha}F^{\ddagger}$ = 6.7 kcal mol^{-1} *vs.* $\Delta_{CH}F^{\ddagger}$ = 5.0 kcal mol^{-1}). In

this case, the concepts applicable to C–H activation and β-hydride in molecular metal complexes are transferable to the interpretation of reactivity at metal nanoparticles.[52]

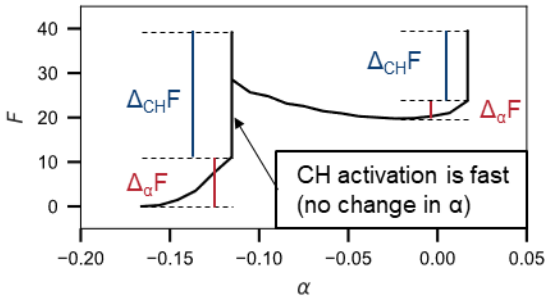

Figure 6. Illustration of the alloy reorganization contribution ($\Delta_\alpha F^\ddagger$) and bond cleavage contribution ($\Delta_{CH}F^\ddagger$) to the free energy barrier of an elementary step.

Propane dehydrogenation on $Pt_{18}Ga_{18}$ (**Figure 7.B**) takes place following a similar mechanism: two subsequent C–H bonds activation at Pt single site to yield propylene, with a higher overall free energy barrier compared to $Ni_{18}Ga_{18}$ ($\Delta F_{Pt}^\ddagger \sim 40$ kcal mol^{-1} *vs.* $\Delta F_{Ni}^\ddagger \sim 25$ kcal mol^{-1}). $Pt_{18}Ga_{18}$ features a different alloying behavior during the reaction compared to $Ni_{18}Ga_{18}$, as suggested by the alloying free energy surfaces (*vide supra*). The first C–H activation, at the central carbon, is preceded by the segregation of Pt which contributes to the barrier ($\Delta_\alpha F^\ddagger = 11.1$ kcal mol^{-1} *vs.* $\Delta_{CH}F^\ddagger = 28.1$ kcal mol^{-1}). After the first C–H activation, further segregation of the alloy occurs. This is consistent with hydride ligands favoring segregated structures (higher α). These large changes in the alloying state are mostly exergonic, and as such do not contribute much to the energy barrier of the second C–H activation ($\Delta_\alpha F^\ddagger = 4.0$ kcal mol^{-1} *vs.* $\Delta_{CH}F^\ddagger = 19.8$ kcal mol^{-1}).

The crucial role played by alloying state dynamics in the mechanism of propane dehydrogenation was further demonstrated by carrying out metadynamics run with identical parameters, but with a constrained alloying state α. In both cases, the reaction follows different mechanisms and the predicted energy barriers are affected (see ESI for details). The metadynamics simulations of propane dehydrogenation over $Ni_{18}Ga_{18}$ and $Pt_{18}Ga_{18}$ suggest that the two alloys behave differently. In $Ni_{18}Ga_{18}$, endergonic alloying is necessary during the second step of the reaction to reduce the electron density at Ni. This reorganization represents an important share of the free energy barrier (~ 50%). On the contrary, $Pt_{18}Ga_{18}$ segregates during the second step, but this segregation is exergonic and has a much smaller impact on the overall free energy barrier. The concept of alloying hardness and skew are appropriate to predict the behavior of the alloys: in hard alloys, the contribution of the alloy reorganization is higher than in soft alloys, while the sign of the skew can predict the direction of the alloying variations. As such, the cost of reorganization during PDH is higher in $Ni_{18}Ga_{18}$ than in $Pt_{18}Ga_{18}$.

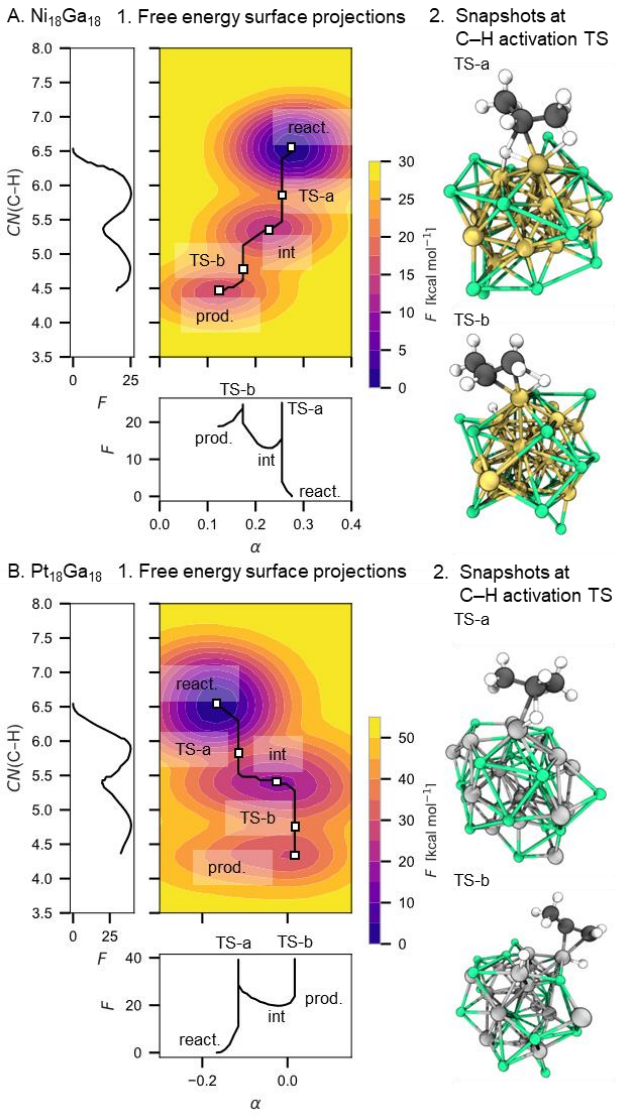

Figure 7. Free energy surface projected along CN(C–H) and α, and free energy profiles projected along each dimension, as obtained from metadynamics simulations (1), snapshots corresponding to the transition state (2.) for $Ni_{18}Ga_{18}$ (**A**) and $Pt_{18}Ga_{18}$ (**B**).

CONCLUSION

In the present study the structures of nanometer-sized clusters were explored using biased AIMD. Biasing the simulations ensures a reliable exploration of large-scale alloy reorganization. The DFT level of theory makes this method more general than parametrized force fields. A set of descriptors, transferable to any alloy, was developed to compare alloying free energy surfaces: the alloy position (α^{min}), the alloying hardness (η) and the alloy's skew (κ).

The Ni-, Pd- and Pt-Ga models have different alloying states, going from hard, core-shell-type alloys (Ni-Ga) to softer alternating to entropic alloys (Pd-, Pt-Ga). Both CO and H_2 ligands alter the alloy position α, its hardness η as well as its skew κ. The alloying state of a given nanoparticle and the changes upon ligand coordination could be interpreted in terms of the relative stability of discrete coordination environments for the group-10-metal, using a principal component analysis methodology.

The alloying parameter α can be used as part of the reaction coordinate to explore the effect of the alloying state on the reactivity of a nanoparticle. In the case of propane dehydrogenation, the variations of α are a crucial part of the reaction coordinate. The different alloys accommodate the elementary steps in different manners, which can be predicted from the previously introduced descriptor set. While the necessary alloying of the hard Ni-Ga during the reaction is endergonic, the dealloying of the soft Pt-Ga is moderately exergonic.

These results highlight the importance of taking alloy reorganization into account when modelling reaction mechanisms in heterogeneous catalysis. Alloying descriptors are also useful to quantify differences in the alloying behavior of different catalytic systems. They are also necessary to encourage the exploration of alloying states, or to monitor alloying changes during reactions. We are convinced that investigating the evolution of the alloying state of complex catalytic systems under operating conditions will bring the deeper understanding required to rationalize the behavior of these systems, and to promote their computer-assisted catalyst design.

ASSOCIATED CONTENT

Videos of the PDH metadynamics simulations
Additional figures.
Extended computational details.
The original CP2k output files are available free of charge.
This material is available free of charge via the Internet at http://pubs.acs.org.

AUTHOR INFORMATION

Corresponding Authors

†.

Author Contributions

QP and AP carried out the calculations under the supervision of MEP, CC and PAP. QP wrote the first draft, and the manuscript was written through contributions of all authors. All authors have given approval to the final version of the manuscript.

Funding Sources

This project was provided with computer and storage resources by GENCI at TGCC on the supercomputer Joliot Curie's ROME partition. We gratefully acknowledge support from the PSMN (Pôle Scientifique de Modélisation Numérique) of the ENS de Lyon, and the Euler cluster of ETH Zurich, for computing resources. QP acknowledges funding by the French Ministry of Higher Eduction and Research (CDSN PhD grant).

ACKNOWLEDGMENT

Dr C. Chizallet (IFPEN), Dr C. Raynaud (Univ Montpelier), Dr. E. Pidko (TU Delft), and Prof. O. Eisenstein (Univ Montpellier) are gratefully acknowledged for advice and fruitful discussions.

REFERENCES

[1] Burch, R. Platinum-Tin Reforming Catalysts I. The Oxidation State of Tin and the Interaction between Platinum and Tin. J. Catal., **1981**, *71*, 348–359. https://doi.org/10.1016/0021-9517(81)90238-4.

[2] Bariås, O. A.; Holmen, A.; Blekkan, E. A. Propane Dehydrogenation over Supported Platinum Catalysts: Effect of Tin as a Promoter. *Catal. Today*, **1995**, *24*, 361–364. https://doi.org/10.1016/0920-5861(95)00059-o.

[3] Nawaz, Z. Light Alkane Dehydrogenation to Light Olefin Technologies: A Comprehensive Review. *Rev. Chem. Eng.*, **2015**, *31*. https://doi.org/10.1515/revce-2015-0012.

[4] Jablonski, E. L.; Castro, A. A.; Scelza, O. A.; de Miguel, S. R. Effect of Ga Addition to Pt/Al2O3 on the Activity, Selectivity and Deactivation in the Propane Dehydrogenation. *Appl. Catal. A: Gen.*, **1999**, *183*, 189–198. https://doi.org/10.1016/s0926-860x(99)00058-7.

[5] Searles, K.; Chan, K. W.; Mendes Burak, J. A.; Zemlyanov, D.; Safonova, O.; Copéret, C. Highly Productive Propane Dehydrogenation Catalyst Using Silica-Supported Ga–Pt Nanoparticles Generated from Single-Sites. *J. Am. Chem. Soc.*, **2018**, *140*, 11674–11679. https://doi.org/10.1021/jacs.8b05378.

[6] Sattler, J. J. H. B.; Gonzalez-Jimenez, I. D.; Luo, L.; Stears, B. A.; Malek, A.; Barton, D. G.; Kilos, B. A.; Kaminsky, M. P.; Verhoeven, T. W. G. M.; Koers, E. J.; Baldus, M.; Weckhuysen, B. M. Platinum-Promoted Ga/Al2O3 as Highly Active, Selective, and Stable Catalyst for the Dehydrogenation of Propane. *Angew. Chem. Int. Ed.*, **2014**, *53*, 9251–9256. https://doi.org/10.1002/anie.201404460.

[7] Web article: **Shaping the future of on-purpose propylene production**

[8] Patent: **US9725382B2**

[9] Patent: **US10065905B2**

[10] Patent: **EP2495228B1**

[11] Patent: **US7235706B2**

[12] Patent: **EP2817276B1**

[13] Purdy, S. C.; Seemakurthi, R. R.; Mitchell, G. M.; Davidson, M.; Lauderback, B. A.; Deshpande, S.; Wu, Z.; Wegener, E. C.; Greeley, J.; Miller, J. T. Structural Trends in the Dehydrogenation Selectivity of Palladium Alloys. *Chem. Sci.*, **2020**, *11*, 5066–5081. https://doi.org/10.1039/d0sc00875c.

[14] Baumgarten, R.; Ingale, P.; Ebert, F.; Mazheika, A.; Gioria, E.; Trapp, K.; Profita, K. D.; Naumann d'Alnoncourt, R.; Driess, M.; Rosowski, F. Controlling the Coke Formation in Dehydrogenation of Propane by Adding Nickel to Supported Gallium Oxide. *ChemCatChem*, **2023**, *16*. https://doi.org/10.1002/cctc.202301261.

[15] He, Y.; Song, Y.; Cullen, D. A.; Laursen, S. Selective and Stable Non-Noble-Metal Intermetallic Compound Catalyst for the Direct Dehydrogenation of Propane to Propylene. *J. Am. Chem. Soc.*, **2018**, *140*, 14010–14014. https://doi.org/10.1021/jacs.8b05060.

[16] Zhu, M.; Ge, Q.; Zhu, X. Catalytic Reduction of CO2 to CO via Reverse Water Gas Shift Reaction: Recent Advances in the Design of Active and Selective Supported Metal Catalysts. *Trans. Tianjin Univ.*, **2020**, *26*, 172–187. https://doi.org/10.1007/s12209-020-00246-8.

[17] Su, X.; Yang, X.; Zhao, B.; Huang, Y. Designing of Highly Selective and High-Temperature Endurable RWGS Heterogeneous Catalysts: Recent Advances and the Future Directions. *J. Energy Chem.*, **2017**, *26*, 854–867. https://doi.org/10.1016/j.jechem.2017.07.006.

[18] Kwak, J. H.; Kovarik, L.; Szanyi, J. Heterogeneous Catalysis on Atomically Dispersed Supported Metals: CO2 Reduction on Multifunctional Pd Catalysts. *ACS Catal.*, **2013**, *3*, 2094–2100. https://doi.org/10.1021/cs4001392.

[19] Wang, Z.; Wang, L.; Cui, Y.; Xing, Y.; Su, W. Research on Nickel-Based Catalysts for Carbon Dioxide Methanation Combined with Literature Measurement. *J.CO_2 Util.*, **2022**, *63*, 102117. https://doi.org/10.1016/j.jcou.2022.102117.

[20] Zhou, W.; Brack, E.; Ehinger, C.; Paterson, J.; Southouse, J.; Copéret, C. Reactivity Switch of Platinum with Gallium: From Reverse Water Gas Shift to Methanol Synthesis. *J. Am. Chem. Soc.*, **2024**, *146*, 10806–10811. https://doi.org/10.1021/jacs.4c01144

[21] Zimmerli, N. K.; Rochlitz, L.; Checchia, S.; Müller, C. R.; Copéret, C.; Abdala, P. M. Structure and Role of a Ga-Promoter in Ni-Based Catalysts for the Selective Hydrogenation of CO2 to Methanol. *JACS Au*, **2024**, *4*, 237–252. https://doi.org/10.1021/jacsau.3c00677

[22] Docherty, S. R.; Phongprueksathat, N.; Lam, E.; Noh, G.; Safonova, O. V.; Urakawa, A.; Copéret, C. Silica-Supported PdGa Nanoparticles: Metal Synergy for Highly Active and Selective CO2-to-CH3OH Hydrogenation. *JACS Au*, **2021**, *1*, 450–458. https://doi.org/10.1021/jacsau.1c00021.

[23] Siddiqi, G.; Sun, P.; Galvita, V.; Bell, A. T. Catalyst Performance of Novel Pt/Mg(Ga)(Al)O Catalysts for Alkane Dehydrogenation. *J. Catal.*, **2010**, *274*, 200–206. https://doi.org/10.1016/j.jcat.2010.06.016

[24] Sun, P.; Siddiqi, G.; Chi, M.; Bell, A. T. Synthesis and Characterization of a New Catalyst Pt/Mg(Ga)(Al)O for Alkane Dehydrogenation. *J. Catal.*, **2010**, *274*, 192–199. https://doi.org/10.1016/j.jcat.2010.06.017.

[25] Tew, M. W.; Miller, J. T.; van Bokhoven, J. A. Particle Size Effect of Hydride Formation and Surface Hydrogen Adsorption of Nanosized Palladium Catalysts: L3 Edge vs K Edge X-Ray Absorption Spectroscopy. *J. Phys. Chem. C*, **2009**, *113*, 15140–15147. https://doi.org/10.1021/jp902542f.

[26] Sumaria, V.; Nguyen, L.; Tao, F. F.; Sautet, P. Atomic-Scale Mechanism of Platinum Catalyst Restructuring under a Pressure of Reactant Gas. *J. Am. Chem. Soc.*, **2022**, *145*, 392–401. https://doi.org/10.1021/jacs.2c10179.

[27] Philippot, K.; Chaudret, B. Organometallic Approach to the Synthesis and Surface Reactivity of Noble Metal Nanoparticles. *C. R. Chimie*, **2003**, *6*, 1019–1034. https://doi.org/10.1016/j.crci.2003.07.010.

[28] Teschner, D.; Révay, Z.; Borsodi, J.; Hävecker, M.; Knop-Gericke, A.; Schlögl, R.; Milroy, D.; Jackson, S. D.; Torres, D.; Sautet, P. Understanding Palladium Hydrogenation Catalysts: When the Nature of the Reactive Molecule Controls the Nature of the Catalyst Active Phase. *Angew. Chem. Int. Ed.*, **2008**, *47*, 9274–9278. https://doi.org/10.1002/anie.200802134.

[29] Van Speybroeck, V. Challenges in Modelling Dynamic Processes in Realistic Nanostructured Materials at Operating Conditions. *Philos. Trans. R. Soc. A-Math. Phys. Eng. Sci.*, **2023**, *381*. https://doi.org/10.1098/rsta.2022.0239.

[30] Morales-García, Á.; Viñes, F.; Gomes, J. R. B.; Illas, F. Concepts, Models, and Methods in Computational Heterogeneous Catalysis Illustrated through CO_2 conversion. *Wiley Interdiscip. Rev. Comput. Mol. Sci.*, **2021**, *11*. https://doi.org/10.1002/wcms.1530.

[31] Sauer, J. The Future of Computational Catalysis. *J. Catal.*, **2024**, *433*, 115482. https://doi.org/10.1016/j.jcat.2024.115482.

[32] Cusinato, L.; del Rosal, I.; Poteau, R. Shape, Electronic Structure and Steric Effects of Organometallic Nanocatalysts: Relevant Tools to Improve the Synergy between Theory and Experiment. *Dalton Trans.*, **2017**, *46*, 378–395. https://doi.org/10.1039/c6dt04207d.

[33] Fleck, M.; Zagrovic, B. Configurational Entropy Components and Their Contribution to Biomolecular Complex Formation. *J. Chem. Theory Comput.*, **2019**, *15*, 3844–3853. https://doi.org/10.1021/acs.jctc.8b01254.

[34] Pavan, L.; Rossi, K.; Baletto, F. Metallic Nanoparticles Meet Metadynamics. *J. Chem. Phys.* **2015**, *143* (18), 184304. https://doi.org/10.1063/1.4935272.

[35] Rossi, K.; Baletto, F. The Effect of Chemical Ordering and Lattice Mismatch on Structural Transitions in Phase Segregating Nanoalloys. *Phys. Chem. Chem. Phys.* **2017**, *19* (18), 11057–11063. https://doi.org/10.1039/C7CP01397C.

[36] Rochlitz, L.; Pessemesse, Q.; Fischer, J. W. A.; Klose, D.; Clark, A. H.; Plodinec, M.; Jeschke, G.; Payard, P.-A.; Copéret, C. A Robust and Efficient Propane Dehydrogenation Catalyst from Unexpectedly Segregated Pt2Mn Nanoparticles. *J. Am. Chem. Soc.* **2022**, *144* (29), 13384–13393. https://doi.org/10.1021/jacs.2c05618.

[37] Baumgärtner, J. F.; Müller, A.; Docherty, S. R.; Comas-Vives, A.; Payard, P.-A.; Copéret, C. Metadynamics Simulations Reveal Alloying-Dealloying Processes During CO2 Hydrogenation with Bimetallic PdGa Nanoparticle Catalysts. ChemRxiv September 29, 2023. https://doi.org/10.26434/chemrxiv-2023-qk5f7-v3.

[38] Payard, P.-A.; Rochlitz, L.; Searles, K.; Foppa, L.; Leuthold, B.; Safonova, O. V.; Comas-Vives, A.; Copéret, C. Dynamics and Site Isolation: Keys to High Propane Dehydrogenation Performance of Silica-Supported PtGa Nanoparticles. *JACS Au*, **2021**, *1*, 1445–1458. https://doi.org/10.1021/jacsau.1c00212.

[39] Laio, A.; Parrinello, M. Escaping Free-Energy Minima. *Proc. Natl. Acad. Sci. U.S.A.* **2002**, *99*, 12562–12566. https://doi.org/10.1073/pnas.202427399.

[40] Ciccotti, G.; Ferrario, M. Blue Moon Approach to Rare Events. *Mol. Simul.* **2004**, *30* (11–12), 787–793. https://doi.org/10.1080/0892702042000270214.

[41] Martínez, L.; Andrade, R.; Birgin, E. G.; Martínez, J. M. PACKMOL: A package for building initial configurations for molecular dynamics simulations. *J. Comput. Chem.* **2009**, *30* (13), 2157–2164. https://doi.org/10.1002/jcc.21224.

[42] Cowley, J. M. An Approximate Theory of Order in Alloys. *Phys. Rev.* **1950**, *77* (5), 669–675. https://doi.org/10.1103/PhysRev.77.669.

[43] Calvo, F.; Mottet, C. Order-Disorder Transition in Co-Pt Nanoparticles: Coexistence, Transition States, and Finite-Size Effects. *Phys. Rev. B* **2011**, *84*, 035409. https://doi.org/10.1103/PhysRevB.84.035409.

[44] Parr, R. G.; Pearson, R. G. Absolute Hardness: Companion Parameter to Absolute Electronegativity. *J. Am. Chem. Soc.* **1983**, *105* (26), 7512–7516. https://doi.org/10.1021/ja00364a005.

[45] Akbarzadeh, H.; Mehrjouei, E.; Abbaspour, M.; Shamkhali, A. N. Melting Behavior of Bimetallic and Trimetallic Nanoparticles: A Review of MD Simulation Studies. *Top. Curr. Chem.* **2021**, *379* (3), 22. https://doi.org/10.1007/s41061-021-00332-y.

[46] Docherty, S. R.; Phongprueksathat, N.; Lam, E.; Noh, G.; Safonova, O. V.; Urakawa, A.; Copéret, C. Silica-Supported PdGa Nanoparticles: Metal Synergy for Highly Active and Selective CO2-to-CH3OH Hydrogenation. *JACS Au*, **2021**, *1*, 450–458. https://doi.org/10.1021/jacsau.1c00021.

[47] McCue, A. J.; Anderson, J. A. CO Induced Surface Segregation as a Means of Improving Surface Composition and Enhancing Performance of CuPd Bimetallic Catalysts. *J. Catal.* **2015**, *329*, 538–546. https://doi.org/10.1016/j.jcat.2015.06.002.

[48] Wang, W. J.; Hwang, S.; Kim, T.; Ha, S.; Scudiero, L. Study of Carbon Supported CuPd Alloy Nanoparticles with Pd-Rich Surface for the Electrochemical Formate Oxidation and CO2 Reduction. *Electrochimica Acta* **2021**, *387*, 138531. https://doi.org/10.1016/j.electacta.2021.138531.

[49] Payard, P.-A.; Rochlitz, L.; Searles, K.; Foppa, L.; Leuthold, B.; Safonova, O. V.; Comas-Vives, A.; Copéret, C. Dynamics and Site Isolation: Keys to High Propane Dehydrogenation Performance of Silica-Supported PtGa Nanoparticles. *JACS Au*, **2021**, *1*, 1445–1458. https://doi.org/10.1021/jacsau.1c00212

[50] Yadav, M.; Szenti, I.; Ábel, M.; Szamosvölgyi, Á.; Ábrahámné, K. B.; Kiss, J.; Zsolt, P.; Sápi, A.; Kukovecz, Á.; Kónya, Z. Concentrated Platinum-Gallium Nanoalloy for Hydrogen Production from the Catalytic Steam Reforming of Ethanol. *ChemCatChem*, **2022**, *15*. https://doi.org/10.1002/cctc.202200717.

[51] Alharis, R. A.; McMullin, C. L.; Davies, D. L.; Singh, K.; Macgregor, S. A. Understanding Electronic Effects on Carboxylate-Assisted C–H Activation at Ruthenium: The Importance of Kinetic and Thermodynamic Control. *Faraday Discuss.*, **2019**, *220*, 386–403. https://doi.org/10.1039/c9fd00063a.

[52] Chaudret, B. Synthesis and Surface Reactivity of Organometallic Nanoparticles. *Top. Organomet. Chem.*, 233–259. https://doi.org/10.1007/b138079.